THE JOURNAL OF PHYSICAL CHEMISTRY C
Article
Cite This: J. Phys. Chem. C 2020, 124, 1197−1206
pubs.acs.org/JPCC

High-Pressure Phase Transitions in Densely Packed Nanocrystallites of TiO_2-II

Xiaoliang Zhang,[†] Hua Tian,[†] Weiwei Li,[†] Weixin Liu,[†] Jian Chen,[†] Junxiu Liu,[†] Xiaoxue Han,[‡] Bingmin Yan,[§] Zhen Chen,[§] Huiyang Gou,[§] Kuo Li,[§] Hui Jiang,[∥] Dongzhou Zhang,[⊥] Martin Kunz,[#] and Hengzhong Zhang*,[†]

[†]Center for High Pressure Science and Technology Advanced Research, Shanghai 201203, China

[‡]State Key Laboratory of Pharmaceutical Biotechnology, Medical School & School of Life Sciences, Nanjing University, Nanjing 210093, China

[§]Center for High Pressure Science and Technology Advanced Research, Beijing 100094, China

[∥]Shanghai Synchrotron Radiation Facility, Shanghai Advanced Research Institute, Chinese Academy of Sciences, Shanghai 201204, China

[⊥]Partnership for Extreme Crystallography Program, University of Hawaii at Manoa, Honolulu, Hawaii 96822, United States

[#]Advanced Light Source, Lawrence Berkeley National Laboratory, Berkeley, California 94720, United States

Supporting Information

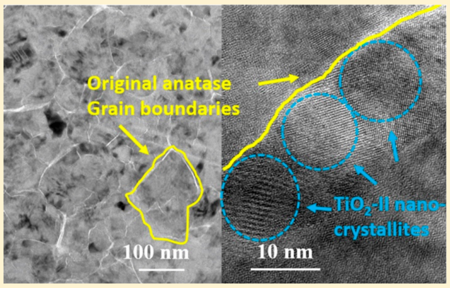

ABSTRACT: Phase behaviors of nanocrystalline TiO_2-II have not been well studied due to the difficulty in its preparations at ambient pressure. In this work, we prepared nanocrystallites of TiO_2-II with average sizes of ∼10−20 nm via high-pressure processing of anatase particles in a large volume press. X-ray diffraction (XRD) and electron microscopy examinations show that the TiO_2-II nanocrystallites formed from cracking and phase transformation of large anatase particles under compression. The high-pressure phase behaviors of the TiO_2-II nanocrystallites were investigated using in situ synchrotron XRD and Raman spectroscopy. Results show that, under compression up to ∼35−40 GPa, the phase transitions in nano TiO_2-II proceed via two parallel routes of TiO_2-II (∼9−15 GPa) → baddeleyite (∼25 GPa) → TiO_2-OI and TiO_2-II (∼19 GPa) → TiO_2-OI. At different TiO_2-II sizes, the TiO_2-II-to-baddeleyite transition occurs at pressures from ∼9 to 15 GPa, while the TiO_2-II-to-TiO_2-OI transition occurs at ∼19 GPa. This difference originates from the different interfacial energies of the involved titania phases, which control their relative thermodynamic phase stabilities at nano sizes. This work enriches our understanding of the complex phase behaviors of titania and provides fundamental knowledge for developing applications of the less-explored titania nanophase of TiO_2-II.

1. INTRODUCTION

Titania (TiO_2) finds applications in photocatalysis,[1−3] coatings,[4] electronic components,[5,6] thermal insulations,[7] etc. TiO_2 has more than 10 polymorphs[8] that include the ambient phases rutile, anatase, brookite, TiO_2(B),[9] TiO_2(H),[10] and TiO_2(R)[11] and the high-pressure phases with the structure types of α-PbO_2 (i.e., TiO_2-II, space group *Pbcn*, ICSD no. 15328[12]), baddeleyite (space group $P2_1/c$, COD no. 9015355[13]), orthorhombic-I (TiO_2-OI, space group *Pbca*, COD no. 9004140[13]), fluorite,[14] cotunnite (TiO_2-OII, space group *Pnma*, ICSD no. 27736[12]), and Fe_2P.[15] It was demonstrated recently that the TiO_2-II phase may have promising applications in photocatalytic and electrocatalytic hydrogen generation[16,17] and in optical and optoelectronic devices due to its high refractive index.[18] Previous studies show that, under compression up to ∼70 GPa, bulk anatase, rutile, and brookite experience the same transition route from bulk TiO_2 phase → TiO_2-II phase → baddeleyite phase → TiO_2-OI phase → TiO_2-OII phase.[19−22] For nanocrystals of titania, the pressure-induced phase transition is dependent on particle size, morphology, and temperature.[23−29] For example, anatase nanocrystals with sizes < ∼10 nm transform to an amorphous state at $P > 27$ GPa and those with sizes between ∼12 and 50 nm transform to the baddeleyite phase at $P > 18$ GPa.[27] In comparison, bulk anatase crystals transform to TiO_2-II at $P > 4.5$ GPa.[30] Interestingly, in decompression to ambient pressure, all high-pressure phases transform to (or retain) the TiO_2-II phase, irrespective of the structures and sizes of the starting phases (e.g., anatase, rutile, or brookite),[19−31] with the exception that an amorphous phase may be produced in a rapid decompression of titania crystallites having sizes <8 nm.[24] However, so far, the high-pressure behavior of

Received: October 22, 2019
Revised: December 3, 2019
Published: December 3, 2019

ACS Publications

DOI: 10.1021/acs.jpcc.9b09932
J. Phys. Chem. C 2020, 124, 1197−1206

nanocrystalline TiO_2-II has been scarcely studied because of the difficulty in synthesizing nano TiO_2-II at ambient pressure. Nonetheless, such a knowledge on the phase behavior of nano TiO_2-II is highly needed for making good use of its material properties for novel applications, such as for photocatalysis[16] and electrocatalysis.[17] Thus, in this work, we used in situ high-pressure (HP) X-ray diffraction (XRD) and HP-Raman spectroscopy to study the structural changes of TiO_2-II nanocrystallites produced from high-pressure processing. Further, we analyzed the size-dependent phase transition behaviors of TiO_2-II using thermodynamics. The obtained knowledge will be indispensable for exploiting new applications of nano TiO_2-II.

2. EXPERIMENTAL SECTION

2.1. Chemicals. Three titanium dioxide (in anatase phase) powders with factory-labeled particle sizes of 40 nm (99.8% wt), 120 nm (99.8% wt), and 2−3 μm (99% wt) were purchased from Macklin Biochem. Co. Ltd. (Shanghai).

2.2. Preparation of TiO_2-II Samples under High-Pressure and High-Temperature (HPHT) Conditions. TiO_2-II samples were prepared from HPHT processing of anatase powders using a multianvil large-volume press (LVP) (Mavo Press LP1000). First, about 0.1 g of powders of a purchased anatase chemical were loaded to the sample chamber (diameter 3 mm) of a zirconia octahedron with a length of 8 mm. Then, the octahedron was assembled to the LVP. The pressure of the LVP was calibrated using the resistance changes associated with the high-pressure phase transitions of ZnS and GaAs.[32] After compressing the sample to ∼15 GPa, the temperature was ramped from room temperature to 350 °C at a rate of 50 °C/min and kept at the temperature for 2 h. Then, the sample was quenched to ambient temperature and pressure. The final product was shaped in a compacted rod (∼ϕ 2.5 mm × L3 mm) consisting of TiO_2-II nanocrystallites (see below). The average crystallite size (see below) of the TiO_2-II sample derived from the factory-labeled "120 nm" anatase was 10.7 nm (herein denoted as sample #1), that from the factory-labeled "2−3 μm" anatase was 17.9 nm (denoted as sample #2), and that from the factory-labeled "40 nm" anatase was 20.2 nm (denoted as sample #3).

2.3. Characterizations of Raw Anatase Samples and As-Prepared TiO_2-II Samples. XRD patterns of the raw anatase samples and the as-prepared TiO_2-II samples were collected using an X-ray diffractometer (Malvern Panalytical) operated at 40 kV and 40 mA, with a Cu Kα radiation (X-ray wavelength 1.54056 Å). The average crystallite sizes of the samples were derived from Rietveld fitting using the Maud program.[33,34]

The morphologies of the crystallites contained in the samples were examined using a scanning electron microscope (SEM) (FEI Versa 3D dual-beam FIB/SEM) operated at 5.0 kV. The elemental distributions in the samples were mapped using energy dispersive spectroscopy (EDS) of the SEM operated at 15.0 kV. The focused ion beam (FIB) accessory of the SEM was used to prepare the specimen for observing the microstructures of the TiO_2-II crystallites using a transmission electron microscope (TEM). The TiO_2-II nanocrystallites contained in the as-prepared TiO_2-II samples and the samples quenched from chosen high pressures (see below) were examined using a JEOL 2100 TEM operated at 200 kV.

2.4. Phase Behavior of TiO_2-II by in Situ High-Pressure X-ray Diffraction. A diamond anvil cell (DAC) was used to generate high pressures on a studied sample. The culet size (diameter) of the anvils was 300 μm. A T301 stainless steel gasket was preindented to ∼30 μm in thickness using the DAC, and a hole of ∼120 μm in diameter was drilled through the center of the indentation using a laser mill, serving as the sample chamber. Another DAC with a culet size of 600 μm was used to compress a sample to ∼15 μm in thickness. A piece of thus compressed sample ∼40 μm in diameter was picked out and loaded into the sample chamber of the first DAC together with two small grains of ruby as the pressure calibrant.[35] Then, neon as the pressure transmitting medium was loaded into the sample chamber using a gas-loading system.

High-pressure XRD of the 10.7 nm TiO_2-II sample #1 (at P up to 35.3 GPa) was performed at the BL15U1 beamline station of Shanghai Synchrotron Radiation Facility (SSRF) at room temperature. XRD patterns were collected at a photon energy of 20 keV (wavelength 0.6199 Å) using a MAR165 CCD detector. The sample-to-detector distance was calibrated using a CeO_2 powder standard.

High-pressure XRD of the 17.9 nm TiO_2-II sample #2 (at P up to 41.5 GPa) was performed at the experimental station 13-BM-C at the GSECARS beamline of Advanced Photon Source (APS). The diffraction was performed at room temperature. XRD patterns were collected at a photon energy of 28.6 keV (wavelength 0.4340 Å) using a MAR165 CCD detector. The sample-to-detector distance and the detector tilt were calibrated using a NIST LaB_6 powder standard.

High-pressure XRD of the 20.2 nm TiO_2-II sample #3 (at P up to 40.1 GPa) was performed at beamline 12.2.2 station of Advanced Light Source (ALS) at room temperature. XRD patterns were collected at a photon energy of 25 keV (wavelength 0.4959 Å) using a MAR345 image plate detector. The sample-to-detector distance was calibrated using a CeO_2 powder standard.

All diffraction images were converted to the intensity versus 2θ data using the Dioptas program.[36] Then, the phases present, the phase contents, and the lattice parameters of all involved TiO_2 phases were identified and/or derived from Rietveld analyses of the XRD data using the Maud program.[33,34]

2.5. Phase Behaviors of TiO_2-II by in Situ High-Pressure Raman Spectroscopy. Raman spectroscopy of TiO_2-II samples at high pressure (up to ∼42 GPa) was measured at room temperature using a Raman spectrometer (inVia Refiex, Renishaw) with a 532 nm-wavelength excitation laser. For a sample at a given pressure, a laser beam of ∼10 μm in diameter was focused at chosen locations of the sample in the DAC and the spectra in the Raman shift range of 100−1250 cm^{-1} were collected and then averaged.

3. RESULTS

3.1. Average Crystallite Sizes of Raw Anatase Samples. The average crystallite sizes (see Table S1, Supporting Information) of the three raw anatase samples were estimated to be 35.0, 326.9, and 416.0 nm based on Rietveld fitting of the XRD patterns (see Figure S1a−d). The latter two sizes (>100 nm) are regarded as inaccurate due to use of narrow XRD peak broadening in the size estimations.[37] To compensate for this shortcoming, SEM images (Figure S2a−c) were used to estimate the average sizes of the crystallites contained in each of the three samples, as listed in

Table S1. It is seen that the nominally 40 nm-sized sample shows good agreement of the SEM size (34.5 nm) with the Rietveld-derived size (35 nm). The medium-sized sample (nominally 120 nm) was measured by SEM to be 122.0 nm, i.e., very close to the nominal size. However, the factory-labeled "2−3 μm" anatase actually has an average crystallite size of 117.5 nm, as determined by SEM. The factory-labeled size might be the aggregate size of anatase nanoparticles.

3.2. Average Crystallite Sizes of As-Prepared TiO_2-II Samples.

The average crystallite sizes of the three as-prepared TiO_2-II samples (see Table S2) were estimated to be 10.7 ± 0.1 nm (sample #1), 17.9 ± 0.2 nm (sample #2), and 20.2 ± 0.1 nm (sample #3) based on Rietveld fitting of the XRD patterns (see Figure S3). TEM images (Figure S4) show that the TiO_2-II samples consisted of densely packed nanocrystallites of TiO_2-II due to application of high pressure during the HPHT syntheses, and the estimated crystallite sizes [∼(10−20) ± (2−4) nm] and size distributions (Figure S4d) are in good agreement with those derived from the XRD data (Table S2). The crystallite sizes of the prepared TiO_2-II samples (∼10−20 nm; Figure S4) are much smaller than those of the raw anatase particles (average size ∼35−120 nm; Figure S2) owing to cracking of the bigger raw anatase crystallites under compression and their subsequent phase transformation to TiO_2-II. It is interesting to note that the smaller the raw anatase crystallites are, the larger the derived TiO_2-II nanocrystallites are (Table S2). This may be attributed to the reduced compressibility and hence the enhanced deformation strength of smaller anatase particles.[38]

The morphologies of the grains contained in the three as-prepared TiO_2-II samples are shown in the SEM images in Figure S5a−c, and the EDS spectra and the elemental mapping of the samples are shown in Figure S5d−f. As with the TEM images (Figure S4a−c), the SEM images show the compacting structure of grains in the as-prepared TiO_2-II samples. EDS spectra show that the TiO_2-II samples consisted of Ti and O atoms with an atomic ratio of Ti:O ≈ 1:2, while EDS elemental mapping shows that Ti and O are uniformly distributed in the samples.

3.3. High-Pressure Phase Behavior of As-Prepared 10.7 nm TiO_2-II.

The XRD patterns of the originally 10.7 nm TiO_2-II (sample #1) at high pressure is shown in Figure 1. It is seen that XRD peaks broaden significantly and, in many cases, overlap with each other due to the small sizes of the involved titania phases. This hinders direct identifications of the phases present. Thus, visual inspections were combined with Rietveld fitting to identify the phases. Representative Rietveld fittings are shown in Figure S6, and the obtained phase contents and lattice parameters are listed in Table S3. Results show that, in compressing to 4.1 GPa, the sample remained as a single phase of TiO_2-II. As the pressure increased to 12 GPa, the baddeleyite phase started to occur. The content of the baddeleyite phase continued to increase with increasing pressure up to the highest experimental value of 35.3 GPa. When the pressure was increased to 21.1 GPa, the TiO_2-OI phase appeared, which remained up to 35.3 GPa. On the other hand, the TiO_2-II phase disappeared at 25.8 GPa. The observed coexistence of baddeleyite and TiO_2-OI at 25.8−35.3 GPa may be attributed to the similarities between the two phases.[39,40] This is because, as shown in Figure 2, both phases comprise regular or slightly distorted augmented triangular prisms[8] each of which consists of one Ti atom coordinated by seven O atoms (Figure 2a,c), and both phases produce similar motifs with open channels along the [001] direction (Figure 2b,d). In decompression, the TiO_2-OI phase fully converted back to the baddeleyite phase at 11.4 GPa, which converted back to the TiO_2-II phase after decompression to ∼0 GPa. These show that the high-pressure phase transitions in TiO_2-II are reversible.

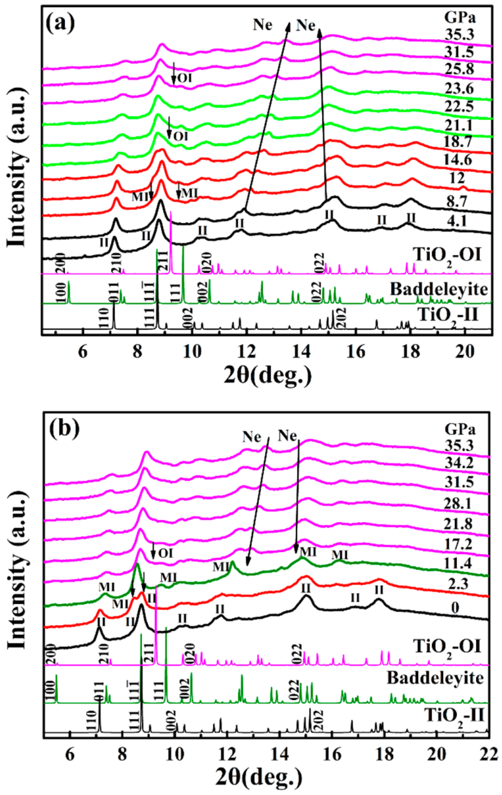

Figure 1. High-pressure XRD patterns of the originally 10.7 nm TiO_2-II (sample #1) under compression (a) and decompression (b) using neon as the pressure transmitting medium. Calculated XRD patterns of TiO_2-II, baddeleyite, and TiO_2-OI are shown at the bottom for comparison. The X-ray wavelength is 0.4340 Å. II = TiO_2-II, MI = baddeleyite, OI = TiO_2-OI.

HP-Raman data (Figure 3) are further used to examine the high-pressure phase transitions in the originally 10.7 nm TiO_2-II. As shown in Figure 3a, the Raman peaks at 0.2 GPa are in good agreement with the predicted vibrational bands of TiO_2-II.[41] When the pressure was increased to 7.6 GPa, a new Raman peak (∼194 cm^{-1}) appeared. This indicates the start of the transition from TiO_2-II to baddeleyite, as this B_u phonon mode of TiO_2-II associates closely with the atomic displacements in TiO_2-II in its transformation to the baddeleyite phase.[41] As the pressure increased to 13.3 GPa, several weak peaks appeared at 219.1, 241.6, and 267.4 cm^{-1}, originating from the characteristic vibrational modes of the baddeleyite phase.[23,41] Upon further compression to 20.4 GPa, the Raman peaks of the TiO_2-OI phase started to occur, while those of the TiO_2-II phase became weak and then almost disappeared at 30.5 GPa. From 30.5 to 40.9 GPa, the Raman spectra contain contributions from both the baddeleyite and TiO_2-OI phases. In decompression (Figure 3b), when the pressure was decreased from 40.9 to 14.1 GPa, the Raman peaks of TiO_2-OI progressively weakened, while those of baddeleyite increased. On further decompression to 12.3 GPa, the Raman peaks were almost all due to the baddeleyite phase. As the pressure was decreased to 3.2 GPa, Raman peaks of

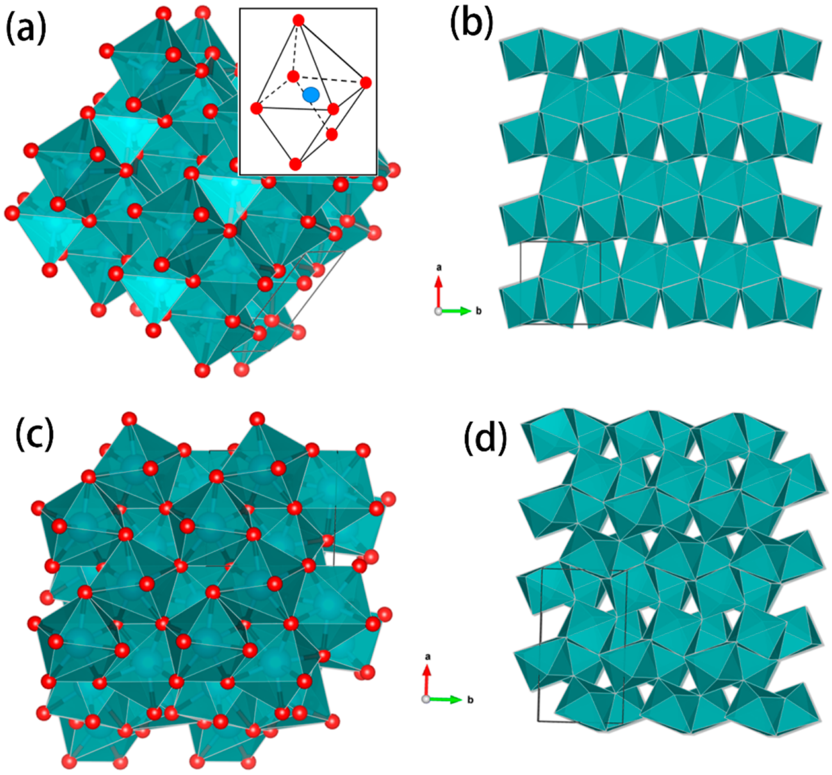

Figure 2. Polyhedron representations of the crystal structures of baddeleyite (a, b) and TiO_2-OI (c, d). Baddeleyite comprises augmented triangular prisms each of which is made of one Ti atom and seven O atoms (a) (see the inset). TiO_2-OI also comprises augmented triangular prisms that are slightly distorted (c). When looking down the [001] direction, both structures produce similar motifs (b, d), indicating their structural similarities.

TiO_2-II became obvious. After the sample is released to the ambient environment (~0 GPa), the Raman spectra can be attributed fully to the single TiO_2-II phase. The observed phase behaviors from the HP-Raman spectroscopy are in good agreement with those from the HP-XRD experiment (above).

3.4. High-Pressure Phase Behavior of As-Prepared 17.9 nm TiO_2-II. As shown in Figure 4a, at high pressure, the phase behaviors of the originally 17.9 nm TiO_2-II (sample #2) are similar to those of the originally 10.7 nm TiO_2-II (sample #1; above). Again, visual inspection combined with Rietveld fitting (Figure S7) was used to identify the phases present and to obtain the phase contents (Table S4). In compression (Figure 4a), the TiO_2-II phase was observed to transform to baddeleyite at 13.7 GPa. As the pressure increased further, the TiO_2-OI phase occurred at 21.9 GPa, whereas the TiO_2-II phase disappeared at 26.3 GPa. Baddeleyite and TiO_2-OI coexisted in the pressure range from 26.3 to 41.5 GPa. In decompression (Figure 4b), the TiO_2-OI phase fully converted back to baddeleyite at 14.7 GPa. Upon further decompressing to 8.0 GPa, the TiO_2-II phase reoccurred. A single phase TiO_2-II was formed when the sample was decompressed to ~0 GPa.

The HP-Raman spectra of the originally 17.9 nm TiO_2-II are shown in Figure 5. In compression (Figure 5a), the phonon mode B_u of TiO_2-II appeared at 7.9 GPa, indicating initiation of its transition to baddeleyite.[41] As the pressure increased to 14.0 GPa, the Raman peaks of the baddeleyite[23,41] phase appeared. Upon further compression to 19.3 GPa, the Raman peaks of the TiO_2-OI phase appeared, whereas the peaks of TiO_2-II became weak and then almost disappeared at 25.4 GPa. In decompression (Figure 5b), when the pressure was decreased to 14.9 GPa, almost all of the Raman peaks came from baddeleyite. As the pressure was further decreased to 8.3 GPa, the TiO_2-II phase appeared, which remained as the only phase when the sample was released to ~0 GPa. The observed phase behaviors from the Raman spectroscopy are consistent with those by the HP-XRD (above).

3.5. High-Pressure Phase Behavior of As-Prepared 20.2 nm TiO_2-II. Representative Rietveld fittings of the HP-XRD patterns of the originally 20.2 nm TiO_2-II (sample #3) are shown in Figure S8, and the derived contents of phases identified are listed in Table S5. In compression (Figure 6a), the TiO_2-II phase started to change to baddeleyite at 16.7 GPa. As the pressure increased further, the TiO_2-OI phase appeared at 22.1 GPa, whereas the TiO_2-II phase disappeared at 29.4 GPa. In the pressure range of 29.4−40.1 GPa, baddeleyite and TiO_2-OI coexisted. In decompression (Figure 6b) from 40.1 down to 15.3 GPa, TiO_2-OI tended to convert back to baddeleyite. When the pressure was decreased to 4.8 GPa, TiO_2-II appeared. After the sample was fully released to the ambient pressure (~0 GPa), a single phase of TiO_2-II was retained.

The HP-Raman spectra of the originally 20.2 nm TiO_2-II are shown in Figure 7. In compression (Figure 7a), the phonon mode B_u of TiO_2-II[41] appeared at 7.7 GPa, similar to those in samples #1 and 2 (above). After the pressure was increased to 20.2 GPa, the Raman peaks of the baddeleyite phase appeared.[23,41] As the pressure was further increased to 21.8 GPa, the Raman peaks of the TiO_2-OI phase started to form, whereas those of TiO_2-II disappeared at 27.0 GPa. From 27.0 to 42.0 GPa, the Raman spectra were contributed from both the baddeleyite and TiO_2-OI phases. In decompression (Figure 7b) from 42.0 to 15.0 GPa, the Raman peaks of TiO_2-OI

DOI: 10.1021/acs.jpcc.9b09932
J. Phys. Chem. C 2020, 124, 1197−1206

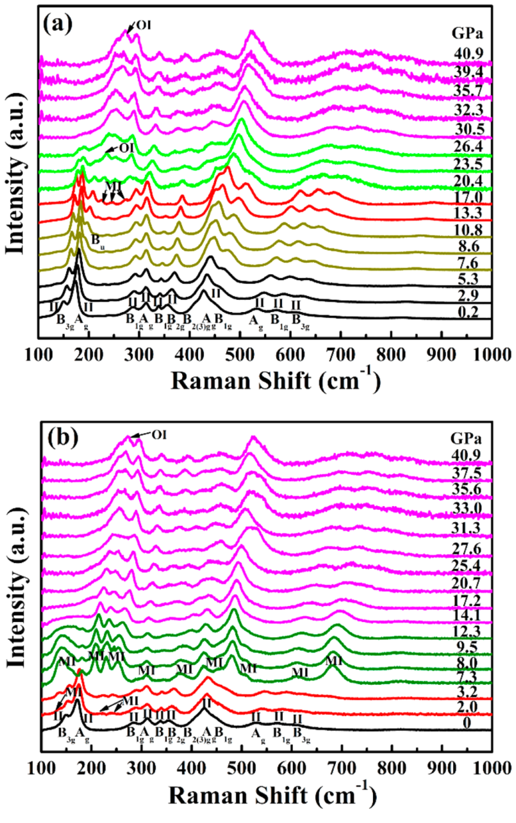

Figure 3. High-pressure Raman spectroscopy of the originally 10.7 nm TiO_2-II (sample #1) under compression (a) and decompression (b). Neon was used as the pressure transmitting medium. II = TiO_2-II, MI = baddeleyite, OI = TiO_2-OI.

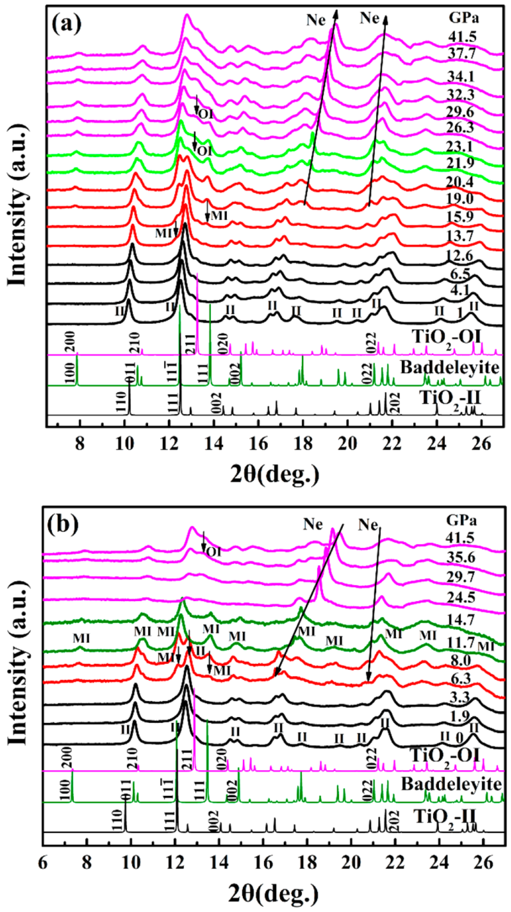

Figure 4. High-pressure XRD patterns of the originally 17.9 nm TiO_2-II (sample #2) under compression (a) and decompression (b) using neon as the pressure transmitting medium. Calculated XRD patterns of TiO_2-II, baddeleyite, and TiO_2-OI are shown at the bottom for comparison. The X-ray wavelength is 0.6199 Å. II = TiO_2-II, MI = baddeleyite, OI = TiO_2-OI.

became weaker, while those of the baddeleyite phase became stronger. At 12.6 GPa, the Raman spectra were almost all from the baddeleyite phase. When the sample was decompressed to 6.0 GPa, the Raman peaks of TiO_2-II appeared. After the sample was fully decompressed to the ambient pressure (~0 GPa), the Raman peaks were all from the TiO_2-II phase. The observed phase behaviors from the Raman spectroscopy are consistent with those by the HP-XRD (above).

3.6. Variations of Contents, Sizes, Lattice Parameters, and Densities of Titania Phases with Pressure. From Rietveld fitting (see the examples in Figures S6−S8) of the HP-XRD data (Figures 1, 4, and 6) of the three TiO_2-II samples under compression (decompression), the phase contents (Figure 8), average crystallite sizes (Figure S9), lattice parameters (Figures S10−S12), and densities (Figure S13) of relevant phases are derived as a function of pressure. The onset pressure of the phase transition from TiO_2-II to baddeleyite (i.e., at the transition point) can be obtained by linear extrapolation of the phase content of baddeleyite to zero (see Figure 8). The transition pressures (~9−15 GPa) thus obtained are listed in Table 1. In the table, listed are also the average crystallite sizes and densities of TiO_2-II determined from Figures S9 and S13, respectively, by reading their respective values at the corresponding transition pressures. The densities of baddeleyite at the transition pressures (Table 1) were calculated from their respective linear-least-squares fittings shown in Figure S13.

Figure 8 also shows that the TiO_2-OI phase started to form at 18.9 (Figure 8a), 19.1 (Figure 8b), and 18.8 GPa (Figure 8c) in the three TiO_2-II samples under compression. After initiation of the formation of TiO_2-OI at the transition pressure in each of the three samples, the phase content of baddeleyite continued to increase, while that of TiO_2-II continued to decrease (Figure 8). This suggests that the formation of TiO_2-OI was controlled primarily by the TiO_2-II-to-TiO_2-OI transition rather than the baddeleyite-to-TiO_2-OI transition. However, after full conversion of TiO_2-II to baddeleyite and/or TiO_2-OI at above ~25 GPa, the phase content of baddeleyite decreased, while that of TiO_2-OI increased (Figure 8), suggesting direct transition from baddeleyite to TiO_2-OI. Thus, there are two parallel phase transition routes in compression of the nano TiO_2-II samples in this study: TiO_2-II (~9−15 GPa) → baddeleyite (~25 GPa) → TiO_2-OI and TiO_2-II (~19 GPa) → TiO_2-OI. In decompression, these transition sequences are reversible (Figure 8).

4. DISCUSSION

4.1. Pressure Dependence of the Average Crystallite Size of TiO_2-II. The average crystallite sizes and microstrains of the TiO_2-II phase in compression of the three TiO_2-II samples are shown in Figure S9. It is seen that the average size of the TiO_2-II phase increases with increasing pressure in sample #1 (Figure S9a), while it decreases with increasing

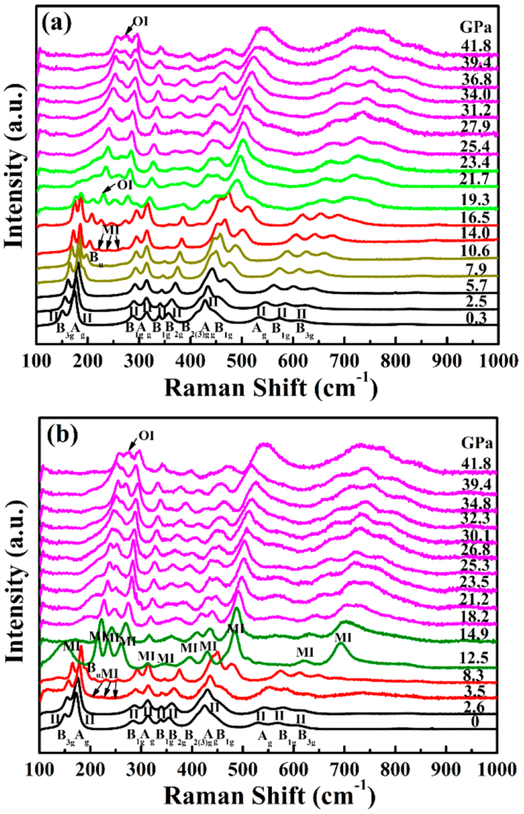

Figure 5. High-pressure Raman spectroscopy of the originally 17.9 nm TiO_2-II (sample #2) under compression (a) and decompression (b). Neon was used as the pressure transmitting medium. II = TiO_2-II, MI = baddeleyite, OI = TiO_2-OI.

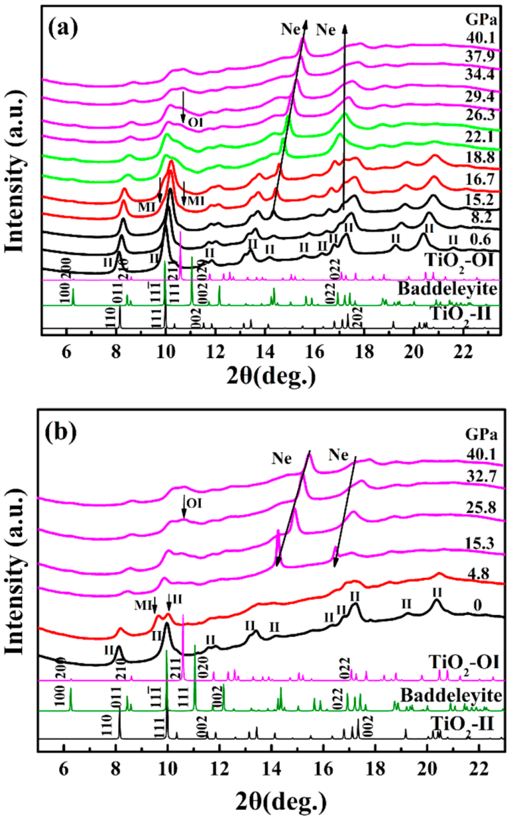

Figure 6. High-pressure XRD patterns of the originally 20.2 nm TiO_2-II (sample #3) under compression (a) and decompression (b) using neon as the pressure transmitting medium. Calculated XRD patterns of TiO_2-II, baddeleyite, and TiO_2-OI are shown at the bottom for comparison. The X-ray wavelength is 0.4959 Å. II = TiO_2-II, MI = baddeleyite, OI = TiO_2-OI.

pressure in samples #2 and 3 (Figure S9c and e). Under compression to high pressures, there are several factors that can affect the average sizes of highly packed nanocrystallites. With an increase in pressure, nanocrystallites may undergo elastic and then plastic deformation, depending on the magnitude of the applied pressure. The former can shrink the crystallite elastically, while the latter can cause cracking of the crystallites. Both factors would produce smaller crystallite sizes with increasing pressure, as seen in Figure S9c and e. On the other hand, if adjacent nanocrystallites happen to have similar crystallographic orientations, under compression, they may join to form one or more bigger crystallites via orientated attachment.[42,43] This would produce increased crystallite sizes with increasing pressure, as seen in Figure S9a. Parts b, d, and f of Figure S9 show that, with an increase in pressure, the microstrain increases, which can be attributed to the increased structural distortions in the nanocrystallites induced by high pressure.

In order to examine the microstructures of the samples at high pressure, samples #1−3 were compressed in a DAC to their respective transition pressures (Table 1) in a neon pressure medium and then quenched to ambient pressure for TEM examinations. TEM images (Figure S14) reveal that, in the quenched samples, many original grain boundaries formed among raw anatase particles were retained, while small TiO_2-II crystallites were contained within the original grain boundaries. This once again confirms the formation of the TiO_2-II nanocrystallites from cracking and phase transition of the raw anatase particles. The average crystallite sizes (Table S6) and the size distributions (Figure S14d) derived from the TEM images are in good agreement with the sizes derived from the Rietveld fittings (Table 1).

4.2. Thermodynamic Analyses of the Size Effect on Pressure-Induced Phase Transitions.

Table 1 shows that the transition pressure from TiO_2-II to baddeleyite changes appreciably with the average crystallite size of TiO_2-II. It has been shown previously that the size dependence of the phase transition temperature and/or pressure in nanoparticles can be analyzed using classic thermodynamics.[44,45] According to ref 45, at a constant temperature, the free energy change in transition from a nanophase α (here, TiO_2-II) to a nanophase β (here, baddeleyite) can be written as

$$\begin{aligned}
&\Delta G(\text{nano-}\alpha \rightarrow \text{nano-}\beta)\\
&\quad = \Delta G(\infty\text{-}\alpha \rightarrow \infty\text{-}\beta) + (\text{surface free energy}\\
&\quad\quad \text{and surface pressure contributions})\\
&\quad = \Delta G^\circ(\infty, T) + \Delta V(P - P_0) + 2(2t + 3)\\
&\quad\quad \times M\left(\frac{\gamma_\beta}{D_\beta\rho_\beta} - \frac{\gamma_\alpha}{D_\alpha\rho_\alpha}\right)\\
&\quad = \Delta G^\circ(\infty, T) + \Delta V(P - P_0) + 10M\left(\frac{\gamma_\beta}{D_\beta\rho_\beta} - \frac{\gamma_\alpha}{D_\alpha\rho_\alpha}\right)
\end{aligned} \quad (1)$$

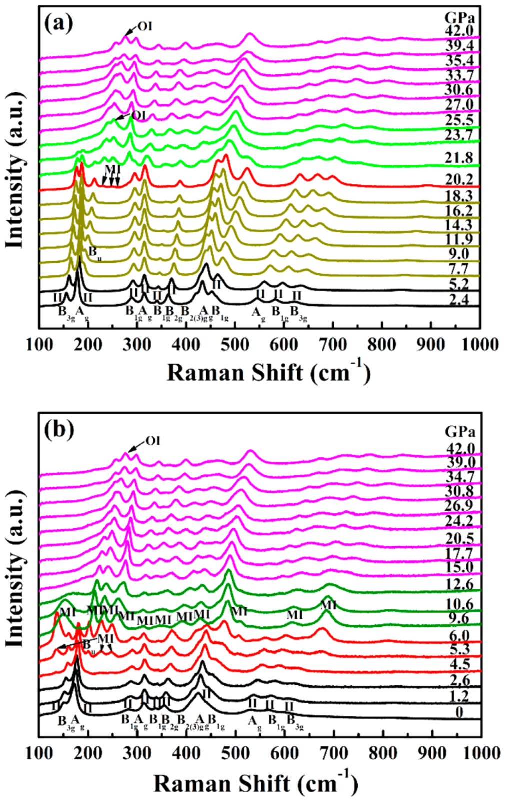

Figure 7. High-pressure Raman spectroscopy of the originally 20.2 nm TiO_2-II (sample #3) under compression (a) and decompression (b). Neon was used as the pressure transmitting medium. II = TiO_2-II, MI = baddeleyite, OI = TiO_2-OI.

In the above equation, $\Delta G^\circ(\infty, T)$ is the free energy change from a bulk α-phase to a bulk β-phase; T is the temperature; P is the pressure (P_0 is the ambient pressure, ~0 GPa); M is the molecular weight of TiO_2 (79.9 g/mol); ΔV is the difference in the molar volumes of the two nanophases; t is a coefficient close to 1; and γ, D, and ρ are the interfacial energy, the diameter, and the density of a nanophase (α or β). Rigorously, γ is a function of crystallite size at a given temperature and pressure. However, it was shown that γ is insensitive to the size at larger particle sizes (e.g., > ~10 nm for anatase)[46] and hence we treat γ as a constant in this work. ΔV can be calculated from

$$\Delta V = M\left(\frac{1}{\rho_\beta} - \frac{1}{\rho_\alpha}\right) \tag{2}$$

Thermodynamically, for occurrence of the nano TiO_2-II-to-baddeleyite transition, the free energy change (left-hand side of eq 1) must be ≤0. Upon initiation of the phase transition (i.e., at the transition point), the free energy change equals zero. Further, as the densities of TiO_2-II and baddeleyite are close at the transition point (see Table 1), we treat $D_\alpha = D_\beta = D$. With these considerations, by substituting eq 2 into eq 1 and letting the left-hand side of eq 1 equal zero, we obtain the following relationship

$$\begin{aligned}\gamma_\alpha\rho_\beta - \gamma_\beta\rho_\alpha - \rho_\alpha\rho_\beta D\frac{\Delta G^\circ(\infty, T)}{10M} \\ = D(P_{\text{nano}} - P_0)(\rho_\alpha - \rho_\beta)/10\end{aligned} \tag{3}$$

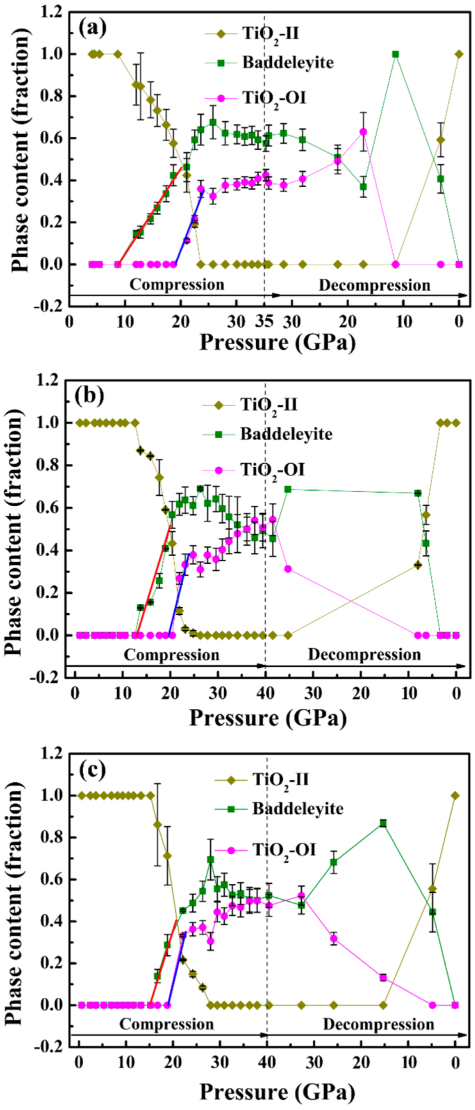

Figure 8. Pressure dependences of the phase contents of various TiO_2 phases present in compression and decompression of the originally (a) 10.7 nm (sample #1), (b) 17.9 nm (sample #2), and (c) 20.2 nm (sample #3) TiO_2-II. Neon was used as the pressure transmitting medium.

Table 1. Properties of Phases at the TiO_2-II-to-Baddeleyite Phase Transition Point

sample no.	average size of TiO_2-II (nm)	density of TiO_2-II (g/cm^3)	density of baddeleyite (g/cm^3)	transition pressure (GPa)
1	11.0 ± 0.2[a]	4.480	4.780	8.7
2	12.4 ± 0.4	4.573	4.901	13.2
3	13.1 ± 0.5	4.607	4.935	15.4

[a] Standard deviation.

or

$$P_{\text{nano}} - P_0 = \frac{10(\gamma_\alpha\rho_\beta - \gamma_\beta\rho_\alpha)}{D(\rho_\alpha - \rho_\beta)} + \frac{\rho_\alpha\rho_\beta}{\rho_\beta - \rho_\alpha}\frac{\Delta G^\circ(\infty, T)}{M} \tag{4}$$

where P_{nano} represents the transition pressure in a nanophase. For a transition at the bulk sizes, $D \to \infty$ and eq 4 becomes

$$P_\infty - P_0 = \frac{\rho_\alpha \rho_\beta}{\rho_\beta - \rho_\alpha} \frac{\Delta G^\circ(\infty, T)}{M} \tag{5}$$

where P_∞ represents the transition pressure in a bulk phase. Subtracting eq 5 from eq 4, one obtains

$$P_{\mathrm{nano}} - P_\infty = -\frac{10}{D} \frac{\left(\frac{\gamma_\beta}{\rho_\beta} - \frac{\gamma_\alpha}{\rho_\alpha}\right)}{\left(\frac{1}{\rho_\beta} - \frac{1}{\rho_\alpha}\right)} \tag{6}$$

Using known quantities at the transition points for the three TiO_2-II samples (Table 1), three concurrent equations can be established in the form of eq 3. Thus, the three unknown quantities γ_α, γ_β, and $\Delta G^\circ(\infty, T)$ can be derived: $\gamma_\alpha = 3.61$ J/m^2, $\gamma_\beta = 0.96$ J/m^2, and $\Delta G^\circ(\infty, 298\ \mathrm{K}) = 53675.6$ J/mol. Understandably, the three derived quantities may have large uncertainties, as the number (three) of the established concurrent equations is just equal to the number (three) of unknown variables. Even so, the following term

$$\frac{\gamma_\beta}{\rho_\beta} - \frac{\gamma_\alpha}{\rho_\alpha} \approx -0.6 < 0$$

predicts a decrease of the transition pressure with decreasing crystallite size according to eq 6, consistent with the experimental data (Table 1).

Using the experimentally determined densities (Table 1) and the derived $\Delta G^\circ(\infty, 298\ \mathrm{K})$, the transition pressure from bulk TiO_2-II to bulk baddeleyite was calculated to be ~47 GPa using eq 5. In a previous work, the enthalpies of various TiO_2 phases were calculated as a function of pressure using density-functional theory.[20] Using the enthalpy versus pressure diagram in ref 20, the theoretical transition pressure from bulk TiO_2-II to baddeleyite is ~25 GPa. Thus, the modeling-derived P_∞ (~47 GPa) has the same order of magnitude as the theoretically derived one. The apparent difference between them can be attributed to the potentially high error of $\Delta G^\circ(\infty, 298\ \mathrm{K})$ introduced in its derivation from only three concurrent equations (eq 3).

For the TiO_2-II-to-TiO_2-OI transition, the closeness in the transition pressures (18.9, 19.1, and 18.8 GPa) in the three TiO_2-II samples suggests that

$$\frac{\gamma_\beta}{\rho_\beta} - \frac{\gamma_\alpha}{\rho_\alpha} \sim 0$$

according to eq 1, where α and β denote TiO_2-II and TiO_2-OI, respectively. Taking $\rho_\alpha \sim 4.6$ g/cm^3 (Table 1) and $\rho_\beta \sim 5.3$ g/cm^3,[8] $\gamma_\beta \sim 3.61 \times 5.3/4.6 = 4.2$ J/m^2 according to the above relationship.

The above thermodynamic analyses show that the dissimilar pressure dependences of the phase transitions that occurred in compression of TiO_2-II nanocrystallites stem from the different interfacial energies of the involved phases, which control their thermodynamic stabilities at different sizes.

5. CONCLUSIONS

In this work, we prepared densely packed nanocrystallites of TiO_2-II with average sizes of ~10−20 nm via high-pressure and high-temperature processing of ~35−120 nm anatase particles. Then, using in situ synchrotron XRD and Raman spectroscopy, we studied the phase transitions of the prepared TiO_2-II nanocrystallites at pressures up to ~35−40 GPa at room temperature. It was found that smaller raw anatase particles produced larger TiO_2-II nanocrystallites. Under compression, the pressure-induced phase transitions of the TiO_2-II nanocrystallites follow the routes of nano TiO_2-II (~9−15 GPa) → baddeleyite (~25 GPa) → TiO_2-OI and nano TiO_2-II (~19 GPa) → TiO_2-OI, which are reversible in decompression to the ambient pressure. Thermodynamic analyses show that the decrease in the transition pressure of the TiO_2-II-to-baddeleyite transition with the decrease in the crystallite size originates from the higher interfacial energy of the TiO_2-II phase (3.61 J/m^2) than the baddeleyite phase (0.96 J/m^2). On the other hand, the minor size dependence of the transition pressure of the TiO_2-II-to-TiO_2-OI transition indicates that the two phases have closer interfacial energies (3.6 vs 4.2 J/m^2). This work enriches our understanding of the complex phase behaviors of the TiO_2 system, providing knowledge useful for exploring new applications of the pressure-quenchable TiO_2-II nanophase.

■ ASSOCIATED CONTENT

Ⓢ Supporting Information

The Supporting Information is available free of charge at https://pubs.acs.org/doi/10.1021/acs.jpcc.9b09932.

> Average crystallite sizes of the raw anatase samples and the as-prepared TiO_2-II samples, SEM images and EDS elemental mapping of TiO_2-II samples, representative Rietveld fitting of HP-XRD patterns of TiO_2-II samples, pressure dependence of the crystal size of the TiO_2-II phase, lattice parameters of various TiO_2 phases present in compression and decompression of TiO_2-II samples, densities of TiO_2-II and baddeleyite phases as a function of pressure, and TEM images of TiO_2-II crystallites quenched from the transition point (PDF)

■ AUTHOR INFORMATION

Corresponding Author

*E-mail: hengzhong.zhang@hpstar.ac.cn. Phone: +86-21-80177095.

ORCID

Kuo Li: 0000-0002-4859-6099
Dongzhou Zhang: 0000-0002-6679-892X
Hengzhong Zhang: 0000-0003-2322-2274

Notes

The authors declare no competing financial interest.

■ ACKNOWLEDGMENTS

This research was supported by the National Natural Science Foundation of China (Grant No. 21875005). The high-pressure synchrotron X-ray diffraction was conducted at beamline station 12.2.2 of Advanced Light Source, Lawrence Berkeley National Laboratory, Berkeley, California, USA, beamline station 13-BM-C of Advanced Photon Source, Argonne National Laboratory, Argonne, Illinois, USA, and Beamline station BL15U1 of Shanghai Synchrotron Radiation Facility, Shanghai, China. The sample syntheses made use of a large volume press housed at the State Key Laboratory of Superhard Materials, Jilin University, China. Use of the Advanced Photon Source was supported by the US Department of Energy (DOE), Office of Science, Office of Basic Energy Sciences, under Contract No. DE-AC02-06CH11357. GSECARS is supported by NSF EAR-1634415 and DOE DE-

FG02-94ER14466. 13-BM-C is supported by COMPRES under NSF Cooperative Agreement EAR-1661511. We thank Yanping Yang (HPSTAR) for assistance with SEM sample characterization.

■ REFERENCES

(1) Jin, X.; Yuan, K.; Wang, X.; Zhang, G.; Zhu, L.; Xu, D. High-Efficient Photocatalytic Performance under Visible Light of Functionalized TiO_2 Nanofibers via Steam and Pressure Co-Modification. *J. Phys. Chem. C* **2019**, *123*, 17306−17317.

(2) Wang, Z.; Wang, Y.; Zhang, W.; Wang, Z.; Ma, Y.; Zhou, X. Fabrication of TiO_2(B)/Anatase Heterophase Junctions at High Temperature via Stabilizing the Surface of TiO_2(B) for Enhanced Photocatalytic Activity. *J. Phys. Chem. C* **2019**, *123*, 1779−1789.

(3) Liu, G.; Sun, C.; Cheng, L.; Jin, Y.; Lu, H.; Wang, L.; Smith, S. C.; Lu, G. Q.; Cheng, H. M. Efficient Promotion of Anatase TiO_2 Photocatalysis via Bifunctional Surface-Terminating Ti−O−B−N Structures. *J. Phys. Chem. C* **2009**, *113*, 12317−12324.

(4) Ghosh, S. K. In *Functional Coatings*; Ghosh, S. K., Ed.; Wiley-VCH Verlag GmbH & Co. KGaA: Weinheim, Germany, 2006; pp 1−28.

(5) Liu, J.; Yan, J.; Shi, Q.; Dong, H.; Zhang, J.; Wang, Z.; Huang, W.; Chen, B.; Zhang, H. Pressure Dependence of Electrical Conductivity of Black Titania Hydrogenated at Different Temperatures. *J. Phys. Chem. C* **2019**, *123*, 4094−4102.

(6) Miao, J.; Miyauchi, M.; Simmons, T. J.; Dordick, J. S.; Linhardt, R. J. Electrospinning of Nanomaterials and Applications in Electronic Components and Devices. *J. Nanosci. Nanotechnol.* **2010**, *10*, 5507−5519.

(7) Fan, J. C.; Bachner, F. J.; Foley, G. H.; Zavracky, P. M. Transparent Heat-Mirror Films of TiO_2/Ag/TiO_2 for Solar Energy Collection and Radiation Insulation. *Appl. Phys. Lett.* **1974**, *25*, 693−695.

(8) Zhang, H.; Banfield, J. F. Structural Characteristics and Mechanical and Thermodynamic Properties of Nanocrystalline TiO_2. *Chem. Rev.* **2014**, *114*, 9613−9644.

(9) Marchand, R.; Brohan, L.; Tournoux, M. TiO_2(B) a New Form of Titanium Dioxide and the Potassium Octatitanate $K_2Ti_8O_{17}$. *Mater. Res. Bull.* **1980**, *15*, 1129−1133.

(10) Latroche, M.; Brohan, L.; Marchand, R.; Tournoux, M. New Hollandite Oxides: TiO_2(H) and $K_{0.06}TiO_2$. *J. Solid State Chem.* **1989**, *81*, 78−82.

(11) Akimoto, J.; Gotoh, Y.; Oosawa, Y.; Nonose, N.; Kumagai, T.; Aoki, K.; Takei, H. Topotactic Oxidation of Ramsdellite-Type $Li_{0.5}TiO_2$, a New Polymorph of Titanium Dioxide: TiO_2(R). *J. Solid State Chem.* **1994**, *113*, 27−36.

(12) Hellenbrandt, M. The Inorganic Crystal Structure Database (ICSD)—Present and Future. *Crystallogr. Rev.* **2004**, *10*, 17−22.

(13) Gražulis, S.; Chateigner, D.; Downs, R. T.; Yokochi, A. F. T.; Quirós, M.; Lutterotti, L.; Manakova, E.; Butkus, J.; Moeck, P.; Le Bail, A. Crystallography Open Database−an Open-Access Collection of Crystal Structures. *J. Appl. Crystallogr.* **2009**, *42*, 726−729.

(14) Mattesini, M.; De Almeida, J.; Dubrovinsky, L.; Dubrovinskaia, N.; Johansson, B.; Ahuja, R. High-Pressure and High-Temperature Synthesis of the Cubic TiO_2 Polymorph. *Phys. Rev. B: Condens. Matter Mater. Phys.* **2004**, *70*, 212101.

(15) Dekura, H.; Tsuchiya, T.; Kuwayama, Y.; Tsuchiya, J. Theoretical and Experimental Evidence for a New Post-Cotunnite Phase of Titanium Dioxide with Significant Optical Absorption. *Phys. Rev. Lett.* **2011**, *107*, No. 045701.

(16) Razavi-Khosroshahi, H.; Edalati, K.; Hirayama, M.; Emami, H.; Arita, M.; Yamauchi, M.; Hagiwara, H.; Ida, S.; Ishihara, T.; Akiba, E.; et al. Visible-Light-Driven Photocatalytic Hydrogen Generation on Nanosized TiO_2-II Stabilized by High-Pressure Torsion. *ACS Catal.* **2016**, *6*, 5103−5107.

(17) Edalati, K.; Wang, Q.; Eguchi, H.; Razavi-Khosrohahi, H.; Emami, H.; Yamauchi, M. Impact of TiO_2-II Phase Stabilized in Anatase Matrix by High-Pressure Torsion on Electrocatalytic Hydrogen Production. *Mater. Res. Lett.* **2019**, *7*, 334−339.

(18) Möls, K.; Aarik, L.; Mändar, H.; Kasikov, A.; Niilisk, A.; Rammula, R.; Aarik, J. Influence of Phase Composition on Optical Properties of TiO_2: Dependence of Refractive Index and Band Gap on Formation of TiO_2-II Phase in Thin Films. *Opt. Mater.* **2019**, *96*, 109335.

(19) Dubrovinskaia, N. A.; Dubrovinsky, L. S.; Ahuja, R.; Prokopenko, V. B.; Dmitriev, V.; Weber, H. P.; Osorio-Guillen, J.; Johansson, B. Experimental and Theoretical Identification of a New High-Pressure TiO_2 Polymorph. *Phys. Rev. Lett.* **2001**, *87*, 275501.

(20) Liu, W.; Chen, J.; Zhang, X.; Yan, J.; Hou, M.; Kunz, M.; Zhang, D.; Zhang, H. Pressure-Induced Phase Transitions of Natural Brookite. *ACS Earth Space Chem.* **2019**, *3*, 844−853.

(21) Al-Khatatbeh, Y.; Lee, K. K.; Kiefer, B. Compressibility of Nanocrystalline TiO_2 Anatase. *J. Phys. Chem. C* **2012**, *116*, 21635−21639.

(22) Dubrovinsky, L. S.; Dubrovinskaia, N. A.; Swamy, V.; Muscat, J.; Harrison, N. M.; Ahuja, R.; Holm, B.; Johansson, B. Materials Science: The Hardest Known Oxide. *Nature* **2001**, *410*, 653.

(23) Hearne, G. R.; Zhao, J.; Dawe, A. M.; Pischedda, V.; Maaza, M.; Nieuwoudt, M. K.; Kibasomba, P.; Nemraoui, O.; Comins, J. D.; Witcomb, M. J. Effect of Grain Size on Structural Transitions in Anatase TiO_2: A Raman Spectroscopy Study at High Pressure. *Phys. Rev. B: Condens. Matter Mater. Phys.* **2004**, *70*, 134102.

(24) Swamy, V.; Kuznetsov, A.; Dubrovinsky, L. S.; McMillan, P. F.; Prakapenka, V. B.; Shen, G.; Muddle, B. C. Size-Dependent Pressure-Induced Amorphization in Nanoscale TiO_2. *Phys. Rev. Lett.* **2006**, *96*, 135702.

(25) Li, Q.; Cheng, B.; Yang, X.; Liu, R.; Liu, B.; Liu, J.; Chen, Z.; Zou, B.; Cui, T.; Liu, B. Morphology-Tuned Phase Transitions of Anatase TiO_2 Nanowires under High Pressure. *J. Phys. Chem. C* **2013**, *117*, 8516−8521.

(26) Swamy, V.; Kuznetsov, A. Y.; Dubrovinsky, L. S.; Kurnosov, A.; Prakapenka, V. B. Unusual Compression Behavior of Anatase TiO_2 Nanocrystals. *Phys. Rev. Lett.* **2009**, *103*, No. 075505.

(27) Swamy, V.; Kuznetsov, A.; Dubrovinsky, L. S.; Caruso, R. A.; Shchukin, D. G.; Muddle, B. C. Finite-Size and Pressure Effects on the Raman Spectrum of Nanocrystalline Anatase TiO_2. *Phys. Rev. B: Condens. Matter Mater. Phys.* **2005**, *71*, 184302.

(28) Chang, H. C.; Chang, S. C.; Hung, T. C.; Jiang, J. C.; Kuo, J. L.; Lin, S. H. A. High-Pressure Study of the Effects of TiO_2 Nanoparticles on the Structural Organization of Ionic Liquids. *J. Phys. Chem. C* **2011**, *115*, 23778−23783.

(29) Machon, D.; Le Bail, N.; Hermet, P.; Cornier, T.; Daniele, S.; Vignoli, S. Pressure-Induced Phase Transitions in TiO_2 Rutile Nanorods. *J. Phys. Chem. C* **2019**, *123*, 1948−1953.

(30) Arlt, T.; Bermejo, M.; Blanco, M. A.; Gerward, L.; Jiang, J. Z.; Olsen, J. S.; Recio, J. M. High-Pressure Polymorphs of Anatase TiO_2. *Phys. Rev. B: Condens. Matter Mater. Phys.* **2000**, *61*, 14414.

(31) Shul'ga, Y. M.; Matyushenko, D. V.; Golyshev, A. A.; Shakhrai, D. V.; Molodets, A. M.; Kabachkov, E. N.; Kurkin, E. N.; Domashnev, I. A. Phase Transformations in Nanostructural Anatase TiO_2 under Shock Compression Conditions Studied by Raman Spectroscopy. *Tech. Phys. Lett.* **2010**, *36*, 841−843.

(32) Lv, S. J.; Cui, H. L.; Du, K. The Pressure Performance of a Slide-Style Multianvil Large Volume Press. *Adv. Mater. Res.* **2013**, *834−836*, 1373−1376.

(33) Lutterotti, L.; Bortolotti, M. Object Oriented Programming and Fast Computation Techniques in Maud, a Program for Powder Diffraction Analysis Written in Java. *IUCr: Compcomm Newsletter* **2003**, *1*, 43−50.

(34) Lutterotti, L.; Matthies, S.; Wenk, H. R. MAUD: A Friendly Java Program for Material Analysis Using Diffraction. *IUCr: Newsletter of the CPD* **1999**, *21*, 14−15.

(35) Mao, H. K.; Bell, P. M.; Shaner, J. T.; Steinberg, D. J. Specific Volume Measurements of Cu, Mo, Pd, and Ag and Calibration of the Ruby R1 Fluorescence Pressure Gauge from 0.06 to 1 Mbar. *J. Appl. Phys.* **1978**, *49*, 3276−3283.

(36) Prescher, C.; Prakapenka, V. B. DIOPTAS: A Program for Reduction of Two-Dimensional X-Ray Diffraction Data and Data Exploration. *High Pressure Res.* **2015**, *35*, 223−230.

(37) Jiang, H. G.; Rühle, M.; Lavernia, E. J. On the Applicability of the X-Ray Diffraction Line Profile Analysis in Extracting Grain Size and Microstrain in Nanocrystalline Materials. *J. Mater. Res.* **1999**, *14*, 549−559.

(38) Chen, B.; Zhang, H.; Dunphy-Guzman, K. A.; Spagnoli, D.; Kruger, M. B.; Muthu, D. V. S.; Kunz, M.; Fakra, S.; Hu, J. Z.; Guo, Q. Z.; et al. Size-Dependent Elasticity of Nanocrystalline Titania. *Phys. Rev. B: Condens. Matter Mater. Phys.* **2009**, *79*, 125406.

(39) Desgreniers, S.; Lagarec, K. High-Density ZrO_2 and HfO_2: Crystalline Structures and Equations of State. *Phys. Rev. B: Condens. Matter Mater. Phys.* **1999**, *59*, 8467.

(40) Leger, J. M.; Atouf, A.; Tomaszewski, P.; Pereira, A. S. Pressure-Induced Phase Transitions and Volume Changes in HfO_2 up to 50 GPa. *Phys. Rev. B: Condens. Matter Mater. Phys.* **1993**, *48*, 93.

(41) Cai, Y.; Zhang, C.; Feng, Y. P. Dielectric Properties and Lattice Dynamics of α-PbO_2-type TiO_2: The Role of Soft Phonon Modes in Pressure-Induced Phase Transition to Baddeleyite-type TiO_2. *Phys. Rev. B: Condens. Matter Mater. Phys.* **2011**, *84*, No. 094107.

(42) Banfield, J. F.; Welch, S. A.; Zhang, H.; Ebert, T. T.; Penn, R. L. Aggregation-Based Crystal Growth and Microstructure Development in Natural Iron Oxyhydroxide Biomineralization Products. *Science* **2000**, *289*, 751−754.

(43) Penn, R. L.; Banfield, J. F. Imperfect Oriented Attachment: Dislocation Generation in Defect-Free Nanocrystals. *Science* **1998**, *281*, 969−971.

(44) Banfield, J. F.; Zhang, H. Nanoparticles in the Environment. *Rev. Mineral. Geochem.* **2001**, *44*, 1−58.

(45) Zhang, H.; Banfield, J. Thermodynamic Analysis of Phase Stability of Nanocrystalline Titania. *J. Mater. Chem.* **1998**, *8*, 2073−2076.

(46) Zhang, H.; Chen, B.; Banfield, J. F. The Size Dependence of the Surface Free Energy of Titania Nanocrystals. *Phys. Chem. Chem. Phys.* **2009**, *11*, 2553−2558.

DOI: 10.1021/acs.jpcc.9b09932
J. Phys. Chem. C 2020, 124, 1197−1206